

Simulation of Nanofiltration Mass Transfer for Magnesium and Lithium Separation in Salt Lakes

Yueyu Liu, Tingting Li, Qing Guo, Lili Gao, Shaohua Yin,* and Shiwei Li*

Cite This: *ACS Omega* 2024, 9, 12219–12227

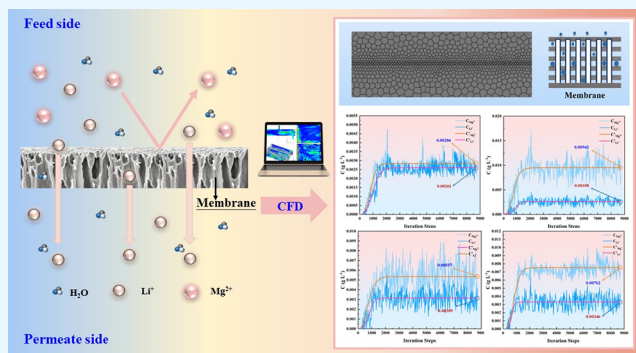
Read Online

ACCESS |

Metrics & More

Article Recommendations

ABSTRACT: A mass transfer model to predict the transport processes of magnesium and lithium ions through porous media in salt lakes has been proposed, which is a combination of the extended Nernst–Planck equation and Donnan effect, accounting for ion diffusion, electromigration, and convection within membrane pores. First, the morphological structure, thickness, surface roughness, and hydrophilicity of the membrane were characterized as fixed parameters, indicating that the surface of the nanofiltration membrane is smooth with low roughness and strong hydrophilicity, resulting in a lower desalination rate but higher water flux. Subsequently, numerical calculations based on the model were conducted to establish a reasonable transport equation for predicting the concentration and retention rate of the main magnesium and lithium ions. When compared with the experimental results, a deviation of less than 5.5% is obtained, confirming the accuracy of the model in describing ion mass transfer. Finally, computational fluid dynamics techniques were employed to simulate the model equations in both the feed and permeate subdomains, demonstrating that the flow characteristics align with reality. Thus, the established transport model exhibits higher predictive accuracy for NF ion separation than one-dimensional models.



1. INTRODUCTION

Lithium, renowned as the “strategic new energy metal of the 21st century”, holds significant importance as a fundamental raw material for chemical energy storage in lithium-ion batteries, crucial in addressing the “dual-carbon” issue.^{1,2} Notably, a substantial portion of China’s lithium resources is extensively dispersed in brines extracted from salt lakes located in Qinghai and Xizang, constituting approximately 87% of the fundamental reserves.³ Of specific concern is the notable high magnesium and lithium ratio (MLR) and low lithium content within Chinese salt lakes. In these lakes, magnesium and lithium ions exhibit similar radii and chemical properties, posing a substantial challenge for effective separation.^{4,5} Hence, the imperative need for the development of a green and efficient lithium extraction technology remains paramount.

In recent years, the application of nanofiltration (NF) technology in lithium extraction from salt lakes has gained considerable traction due to its smaller separation aperture (rp, 0.5–2.0 nm) and suitable molecular weight cutoff (M_w , 200–400 Da).⁶ Compared to conventional methods such as adsorption, chemical precipitation, or solvent extraction, NF is preferred for its advantages of high throughput, environmental friendliness, and low operating pressure.^{7,8} As NF technology advances and diversifies its applications, the underlying separation mechanisms have been progressively investigated and refined.^{9,10} The separation of magnesium and

lithium involves intricate influencing factors and fluidic phenomena. Within this process, the membrane functions as a porous medium, facilitating solute transport in two subdomains: the feed side and the permeate side, driven by diffusion induced by convection and concentration gradients within the pores.¹¹ To accurately depict this process, intricate physical phenomena are continually refined to establish and enhance mass transfer mathematical models. Initially, the Donnan Steric Pore model (DSPM) was introduced by Bowen et al.¹² in 1996 to forecast ion transport. However, the traditional DSPM, a semiempirical model, necessitates membrane characterization through a complex fitting process. Furthermore, the Donnan equilibrium alone fails to elucidate the high rejection rate of multivalent cations, favoring their distribution within the negatively charged membrane.¹³ Dielectric exclusion (DE), serving as an additional distribution effect at the interface between the membrane and the external solution, offers a more comprehensive explanation of mass

Received: January 8, 2024

Revised: February 5, 2024

Accepted: February 9, 2024

Published: February 27, 2024



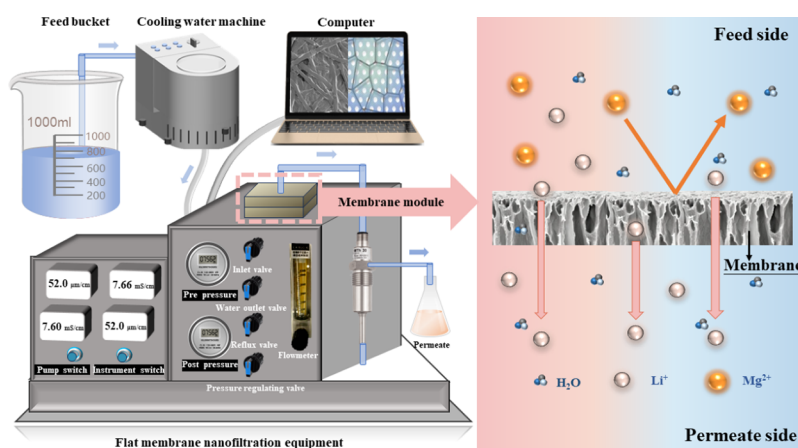


Figure 1. NF separation process flow.

transfer mechanisms in porous media.¹⁴ Consequently, the Donnan Steric Pore and Dielectric Exclusion model (DSPM-DE) was proposed by Schaep et al.¹⁵ to effectively delineate the ion transfer process in NF.

In this study, an advanced mass transfer model has been introduced to anticipate the movement of magnesium and lithium ions across a nanoporous medium. This model integrates the extended Nernst–Planck equation with the Donnan effect, accounting for diffusion, electromigration, and convection simultaneously occurring within the membrane pores. The numerical solution of magnesium and lithium ions mass transport was executed utilizing the developed mass transfer model. Subsequently, the flow and transport mechanisms underwent validation employing the finite element method, providing visual representations for forecasting local ion concentrations, permeate flux, and ion retention within the membrane constituents.

2. EXPERIMENTS AND THEORY

2.1. Experiments and Materials. The NF separation experiments were conducted using a three-stage flat-sheet NF

Table 1. Operating Parameters of the NF Membrane

membrane element	membrane material	pH operating range	operating temperature (°C)
NF90	polyamide	3–10	45
NF270	polyamide	3–10	45
DK	polyamide	2–11	50
DL	polyamide	2–11	50

device. The feed brine was pumped from the raw material barrel to the membrane assembly for membrane separation through a high-pressure pump. The permeate was returned to the raw material barrel to control the feed flow, while the retentate was discharged from the outlet, as illustrated in Figure 1. The commercially available NF membranes (NF90, NF270, DK, and DL) used in the experiments were produced by Guo Chu Technology Co., Ltd. The main operational parameters are detailed in Table 1. The feed solution ratio in the experiments was based on the reference to the Qinghai Chaidamu Salt Lake, with an MLR of 42:1 after a 50-fold dilution. All reagents used were of analytical grade, and magnesium chloride (MgCl₂, anhydrous, AR), lithium chloride

Table 2. Basic Equations of the DSPM-DE Model

Transport equation for a specie *i*

$$j_i = J_v K_{i,c} c_i - D_{i,p} \frac{dc_i}{dx} - z_i c_i D_{i,p} \frac{F}{RT} \frac{d\Psi}{dx} \quad (1)$$

Concentration and potential gradients through the membrane

$$\frac{dc_i}{dx} = \frac{J_v}{D_{i,p}} [K_{i,c} c_i - c_i(\delta^+)] - \frac{z_i F}{RT} \frac{d\Psi}{dx} \quad (2)$$

$$\frac{d\Psi}{dx} = \frac{\sum_{i=1}^n z_i J_v [K_{i,c} c_i - c_i(\delta^+)]}{\frac{F}{RT} \sum_{i=1}^n z_i^2 c_i} \quad (3)$$

Partitioning at membrane/external solution interfaces

$$\frac{c_i(\delta^+)}{c_i(\delta^-)} = \phi_i \exp(-z_i \Delta \Psi_{D0}) \exp(-z_i^2 \Delta W_0) \quad (4)$$

$$\frac{c_i(\delta^-)}{c_i(\delta^+)} = \phi_i \exp(-z_i \Delta \Psi_{D\delta}) \exp(-z_i^2 \Delta W_\delta) \quad (5)$$

Electroneutrality conditions

$$\sum_{i=1}^n z_i c_i(\delta^+) = 0; \sum_{j=1}^n z_j c_j - \chi = 0 \quad (6)$$

Membrane charge density

$$\chi = 10^q c_{ctr}^s c_{ctr} = \frac{1}{2} \sum_{i=1}^n |z_i| c_i(0^-) \quad (7)$$

in which

$$j_i = J_v c_i(\delta^+); D_{i,p} = K_{i,p} D_{i,\infty}; K_{i,d} = K_{i,d}(\lambda_i); \quad (8)$$

$$K_{i,c} = K_{i,c}(\lambda_i); \phi_i = (1 - \lambda_i)^2; \lambda_i = \frac{r_i}{r_p}$$

Mass transfer equation

$$k_a = \frac{J_{v,a}}{\ln\{\Delta p / (\pi_f - \pi_p)[1 - (J_{v,a} / J_{v,H_2O})]\}} \quad (9)$$

(LiCl, anhydrous, AR) were supplied by Tianjin Zhiyuan Chemical Reagent Co., Ltd.

Ion contents in the salt lakes brine were analyzed using inductively coupled plasma optical emission spectroscopy (ICP-OES) (ICAP 6500 DUO, USA). The concentration of organic matter was measured using a total organic carbon (TOC) analyzer (TOC-L, Shimadzu, Japan). The surface morphology of the membrane was observed using scanning electron microscopy (SEM) (Hitachi SU8010, Japan) and atomic force microscopy (AFM) (Shimadzu SPM-9500 J3, Japan).

2.2. Theory. The DSPM-DE model is based on considerations of the DE phenomenon occurring when an ion aqueous solution contacts different media.¹⁶ The transport equation for ion movement is based on the extended Nernst–Planck equation, considering three phenomena: diffusion, electromigration, and convection.¹⁷ It assumes unidirectional transmembrane movement of compounds and an ideal solution.¹⁸ Specifically, the absolute value of the volumetric

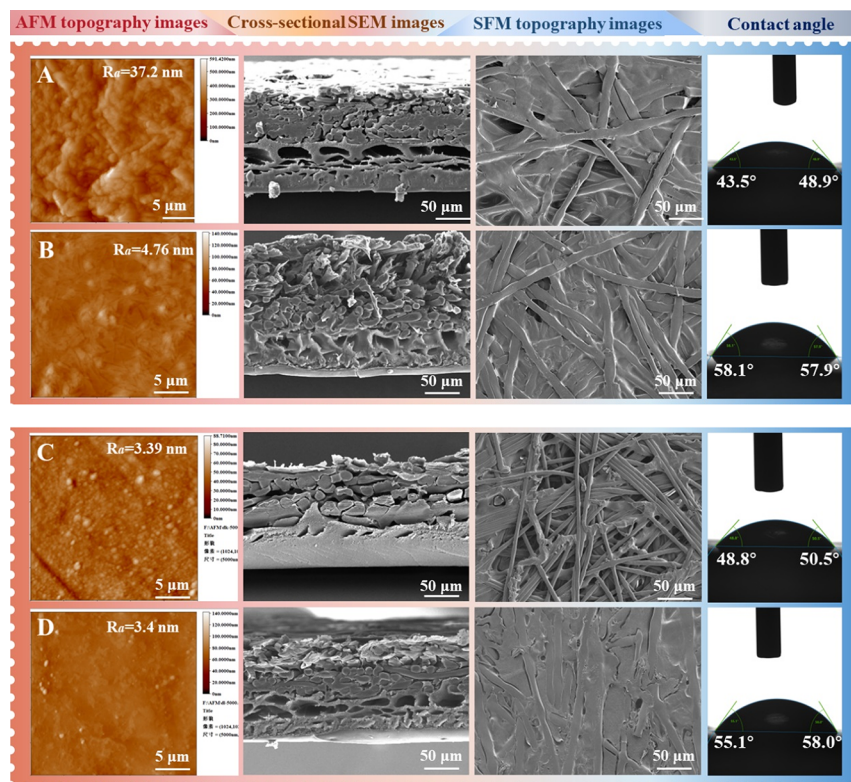


Figure 2. From top to bottom, the AFM morphology image, cross-sectional SEM image, SEM morphology image, and contact angle of the NF membrane are shown in order: (A) NF 90; (B) NF 270; (C) DK; (D) DL.

Table 3. Properties of the System Used in the Simulations

	parameters	values
constant parameters		
$C_{i,f}$	feed concentration of ion i , g L ⁻¹ (Li ⁺ /Mg ²⁺ /Cl ⁻)	5.36/225/115
$C_{i,p}$	permeate concentration of ion i , g L ⁻¹ (Li ⁺ /Mg ²⁺ /Cl ⁻)	NF90 2.75/2.94/97.49 NF270 3.76/9.59/68.80 DK 3.21/5.72/73.13 DL 3.53/7.74/79.20
D_i	diffusivities at infinite dilution, $\times 10^{-9}$ m ² s ⁻¹ (Li ⁺ /Mg ²⁺ /Cl ⁻)	0.813/0.706/2.031
δ	effective membrane thickness, μ m (NF90/NF270/DK/DL)	163/142/117/150
ϵ	porosity (NF90/NF270/DK/DL)	0.38/0.47/0.40/0.43
M_w	molecular weight cutoff, Da (NF90/NF270/DK/DL)	1089/866/947/924
k_a	mass transfer coefficient, $\times 10^{-5}$ m s ⁻¹ (NF90/NF270/DK/DL)	1.05/1.37/1.20/1.28
L_p	membrane permeability, $\times 10^{-14}$ m ³ m ⁻² (NF90/NF270/DK/DL)	1.4/2.4/1.7/2.2
r_p	mean pore radius, $\times 10^{-9}$ m (NF90/NF270/DK/DL)	0.74/0.67/0.70/0.69
Φ_i	equilibrium partition coefficient for steric interactions (Li ⁺ /Mg ²⁺ /Cl ⁻)	NF90 0.24/0.18/0.31 NF270 0.18/0.13/0.28 DK 0.21/0.15/0.28 DL 0.20/0.14/0.27
$K_{i,d}$	hydrodynamic coefficient for hindered transport inside pores (Li ⁺ /Mg ²⁺ /Cl ⁻)	NF90 0.18/0.12/0.23 NF270 0.13/0.08/0.22 DK 0.16/0.11/0.22 DL 0.15/0.10/0.21
$K_{i,c}$	hydrodynamic coefficient accounting for the effect of pore walls on convective transport (Li ⁺ /Mg ²⁺ /Cl ⁻)	NF90 1.33/1.33/1.35 NF270 1.39/1.31/1.36 DK 1.33/1.33/1.36 DL 1.35/1.36/1.33
X	membrane charge density, meq g ⁻¹ (NF90/NF270/DK/DL)	1.6/0.5/1.1/0.7

charge density (χ) is determined as a function of the concentration of counter-ions present at the feed/membrane interface, utilizing a Freundlich isotherm characterized by

parameters s and q [eq (6)]. The basic equation is detailed in Table 2.

Table 4. DSPM-DE Model Equation

nanofiltration	ions	$R_{\text{int}}-J_v$ equation	J_v represents permeation flux, R represents retention rate
NF 90	Mg^{2+}	$j_v = 0.587 \times 10^{-5} \left[-3.902 - \ln \left(\frac{1-R_{\text{int}}}{R_{\text{int}}} \right) \right]$	
	Li^+	$j_v = 0.755 \times 10^{-5} \left[0.300 - \ln \left(\frac{1-R_{\text{int}}}{R_{\text{int}}} \right) \right]$	
NF 270	Mg^{2+}	$j_v = 0.667 \times 10^{-5} \left[-3.341 - \ln \left(\frac{1-R_{\text{int}}}{R_{\text{int}}} \right) \right]$	
	Li^+	$j_v = 0.857 \times 10^{-5} \left[0.770 - \ln \left(\frac{1-R_{\text{int}}}{R_{\text{int}}} \right) \right]$	
DK	Mg^{2+}	$j_v = 0.600 \times 10^{-5} \left[-3.525 - \ln \left(\frac{1-R_{\text{int}}}{R_{\text{int}}} \right) \right]$	
	Li^+	$j_v = 0.767 \times 10^{-5} \left[0.338 - \ln \left(\frac{1-R_{\text{int}}}{R_{\text{int}}} \right) \right]$	
DL	Mg^{2+}	$j_v = 0.607 \times 10^{-5} \left[-3.137 - \ln \left(\frac{1-R_{\text{int}}}{R_{\text{int}}} \right) \right]$	
	Li^+	$j_v = 0.780 \times 10^{-5} \left[0.753 - \ln \left(\frac{1-R_{\text{int}}}{R_{\text{int}}} \right) \right]$	

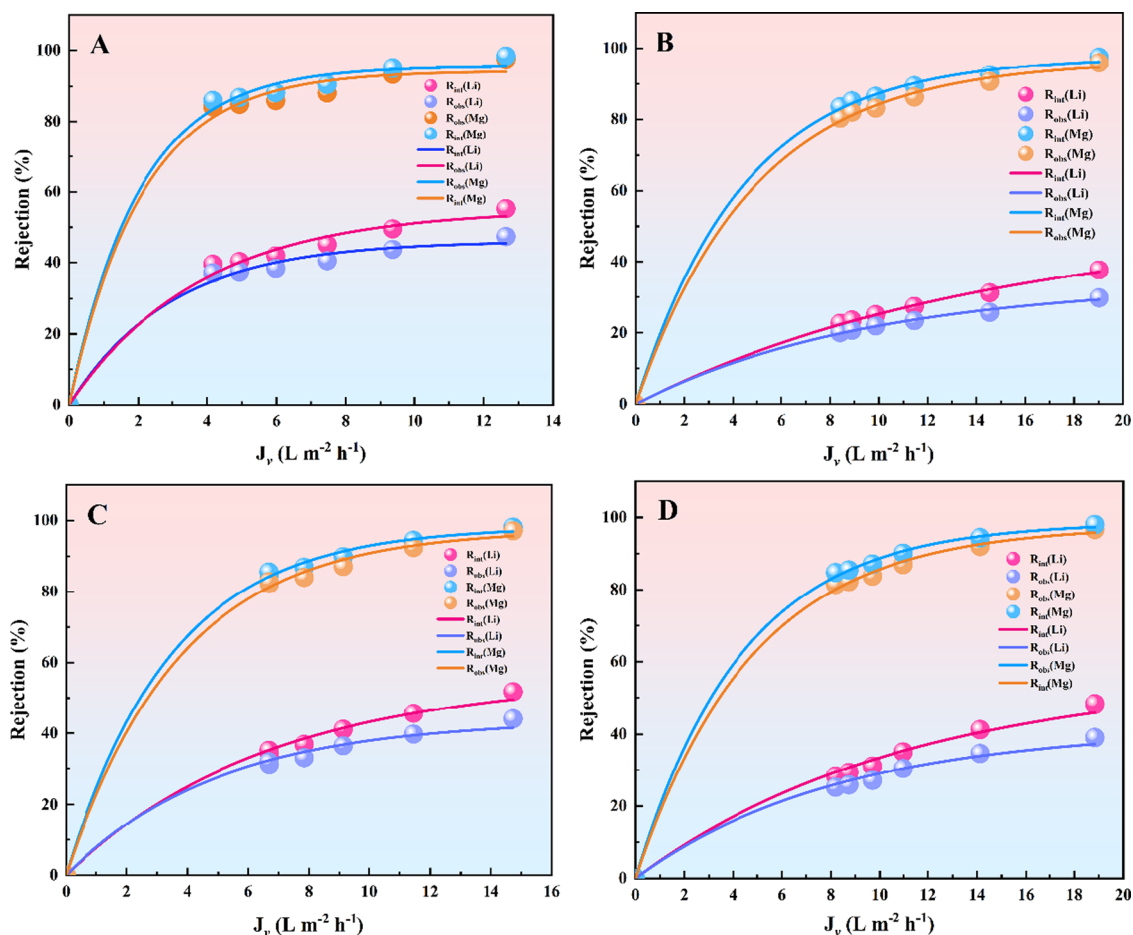


Figure 3. NF of aqueous solutions containing: MgCl_2 , LiCl . Comparison between experimental results and model predictions: (A) NF 90; (B) NF 270; (C) DK; (D) DL. Transmembrane pressure difference = 0.2–3 bar.

In this study, single salt solutions, MgCl_2 and LiCl , were considered separately. It was assumed that ions diffuse at the same rate within the membrane due to their electrical neutrality. Therefore, cations and anions were considered to have the same molecular diffusion rate; i.e., the diffusion rate of the salt is defined as^{19,20}

$$D_{\text{salt}} = \frac{(z_+ + |z_-|)D_+D_-}{z_+D_+ + |z_-|D_-} \quad (10)$$

According to the Boltzmann distribution type, it is postulated that both the membrane and the aqueous phase represent continuous media, wherein the electrostatic effect and polarization charge between ions are taken into consideration.²¹ Furthermore, the impact of DE on the

concentration distribution at the feed/membrane interface for membranes with low dielectric constant values is illustrated by the following equation:²²

$$\Delta W_0 = r_B \left\{ \kappa(0^-) - \kappa(0^+) - \frac{1}{r_p} \ln[1 - \gamma \exp(-2r_p \kappa(0^+))] \right\} \quad (11)$$

The relationship between the concentration distribution of ions crossing the membrane and the membrane thickness is obtained by integrating eq (2) over the membrane thickness, assuming a constant potential gradient across the membrane in the DSPM-DE model.²³

$$c_i(x) = \frac{j_i \delta}{k_i D_{i,p}} + \left[c_i(0^+) - \frac{j_i \delta}{k_i D_{i,p}} \right] \exp\left(k_i \frac{x}{\delta}\right) \quad (12)$$

3. RESULTS AND DISCUSSION

3.1. Characterization of NF Membranes. The structure and geometric parameters (i.e., roughness, contact angle) of

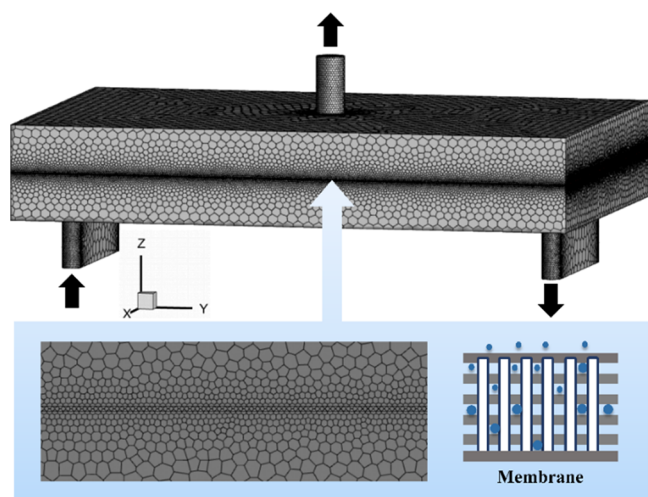


Figure 4. Membrane module structure model and NF discrete membrane interface.

the NF membrane are illustrated in Figure 2, observing that the peaks of the four commercial NF membranes are small and evenly distributed, presenting a typical “ridge and valley” structure. Among them, DK and DL exhibit smaller roughness, and the membrane surfaces are smoother. In contrast, the surface of NF90 is the roughest, more prone to ion accumulation and membrane fouling. At the surface of the membrane, different circular or rod-shaped particle structures

are evident. These structures result from the rapid interface polymerization of the “aqueous phase” and “oil phase” on the surface of the porous support layer during the membrane synthesis process. The particle-rich surface roughness increases the contact probability between the polyamide layer and the feed solution per unit area, thereby enhancing the water flux in the membrane separation process. Additionally, the cross-section of the membrane reveals a porous network in the support layer and an interconnected network of open nanotubes, accelerating the micromixing state of the feed solution on the surface. This structure enhances the dynamic conditions of the fluid and increases the likelihood of turbulence occurring on the surface of the feed solution. Furthermore, contact angle detection reveals that all four commercial NF membranes exhibit strong hydrophilicity, and their hydrophilicity is close, all below 60°. In summary, the surface of the NF membrane is smooth with low roughness and strong hydrophilicity, resulting in a lower desalination rate but higher water flux.

3.2. Numerical Solution of Transmission Model. This study numerically simulates two single salt solutions (MgCl₂ and LiCl) with an MLR of 42:1. The assumption is made that ions diffuse at the same rate due to their electrical neutrality. Operational conditions and physicochemical properties of the model in this study are presented in Table 3. The typical operating parameters include inlet and outlet concentrations, pressure, and flux. Membrane characteristics are crucial inputs to the model, encompassing pore radius, porosity, membrane thickness, and charge density.

To validate the accuracy of the DSPM-DE model, magnesium and lithium ions were selected as target substances. Utilizing MATLAB software, the obtained permeation flux and corresponding R_{int} data were input into the formula for data fitting, leading to the mathematical model equation for the membrane (Table 4). Figure 3 illustrates the comparison between model predictions and experimental results, indicating that the target substances in the study exhibit consistency with the theoretical model, and the experimental results are well reproduced. It is noteworthy that the consideration of the DE effect has been significantly enhanced the prediction of rejection for divalent ions, and the real rejection of ion i is then given by

$$R_{i,obs} = 1 - \frac{C_{i,p}}{C_{i,f}} \quad (13)$$

3.3. Mass Transport in Nanoporous Media. Finite element simulation software was utilized to simulate the transport process, with a cross-flow pattern within the module. The k - ϵ turbulent model and Euler–Lagrange equation were employed, allowing conservation within the mass domain. The

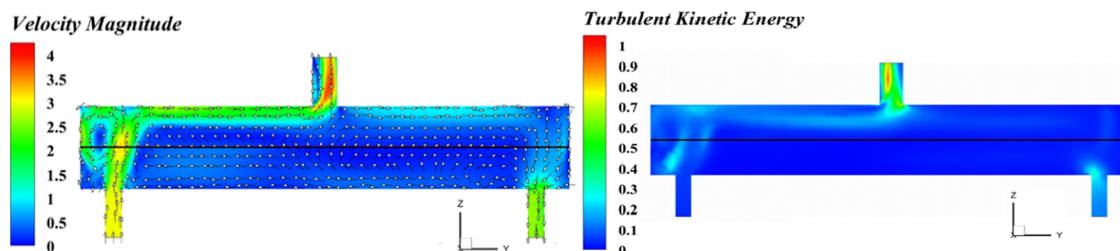


Figure 5. Nephogram of absolute value of NF membrane velocity and turbulent kinetic energy.

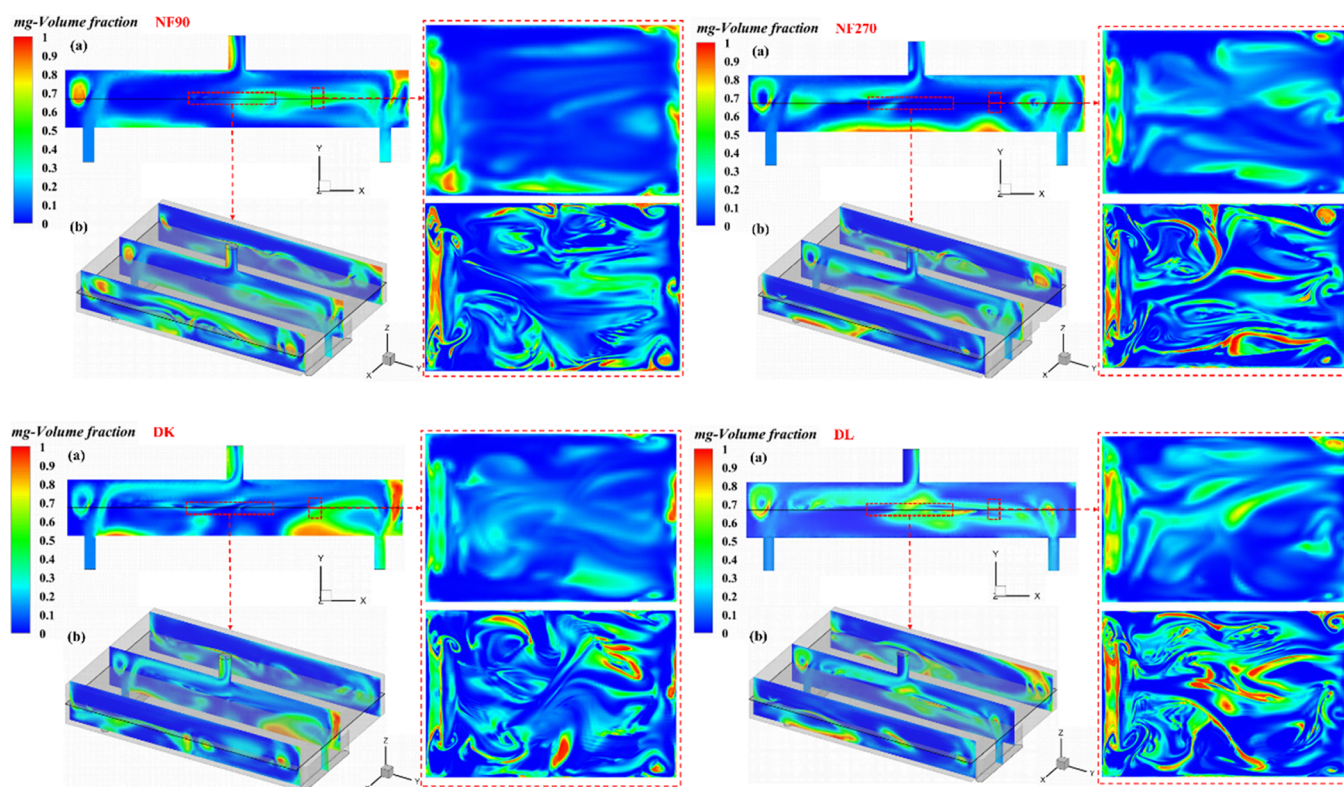


Figure 6. Concentration field distribution cloud image of Mg^{2+} : (a) $x/X = 0$ cross-sectional cloud image, concentration distribution cloud image of the membrane surface on the concentration side, and membrane surface concentration distribution cloud image on the permeation side; (b) overall concentration field cloud image of the NF module.

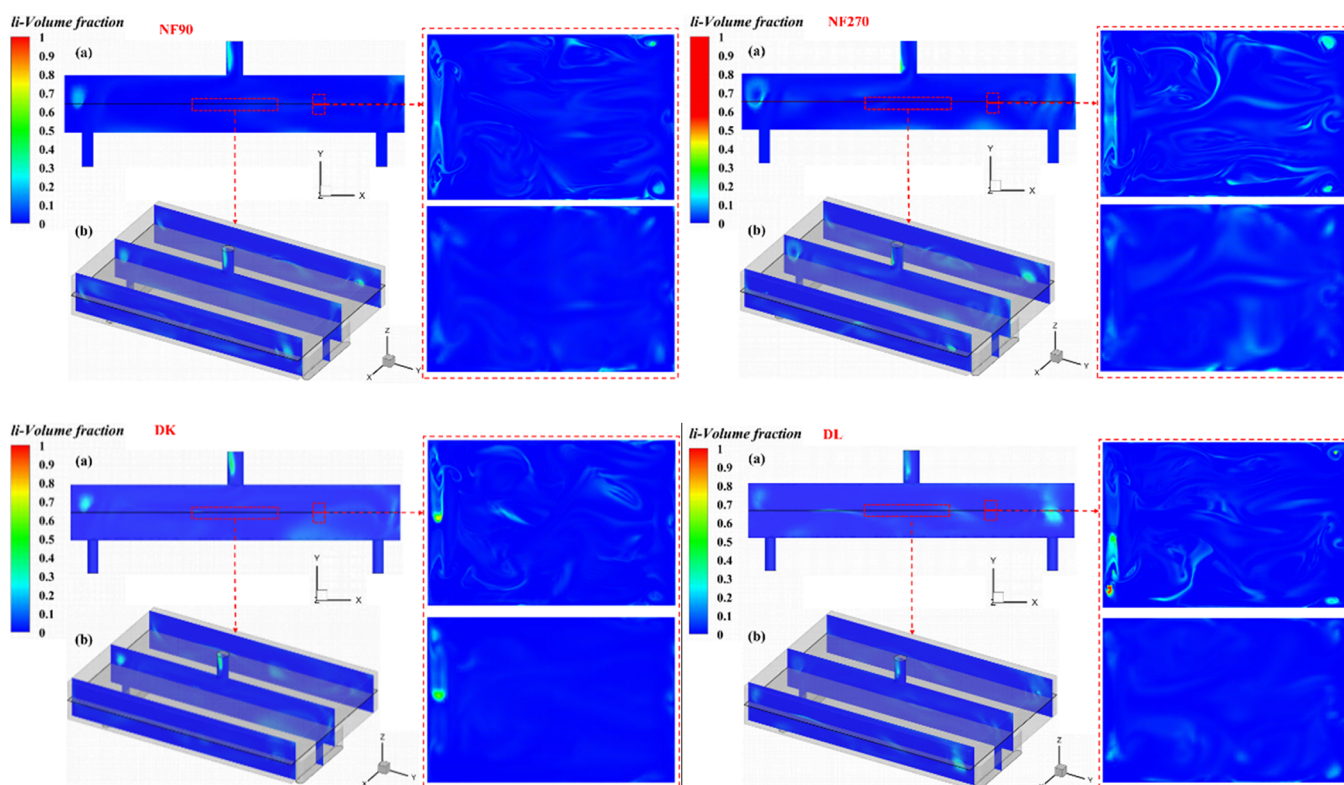


Figure 7. Concentration field distribution cloud image of Li^+ : (a) $x/X = 0$ cross-sectional cloud image, concentration distribution cloud image of the membrane surface on the concentration side, and membrane surface concentration distribution cloud image on the permeation side; (b) overall concentration field cloud image of the NF module.

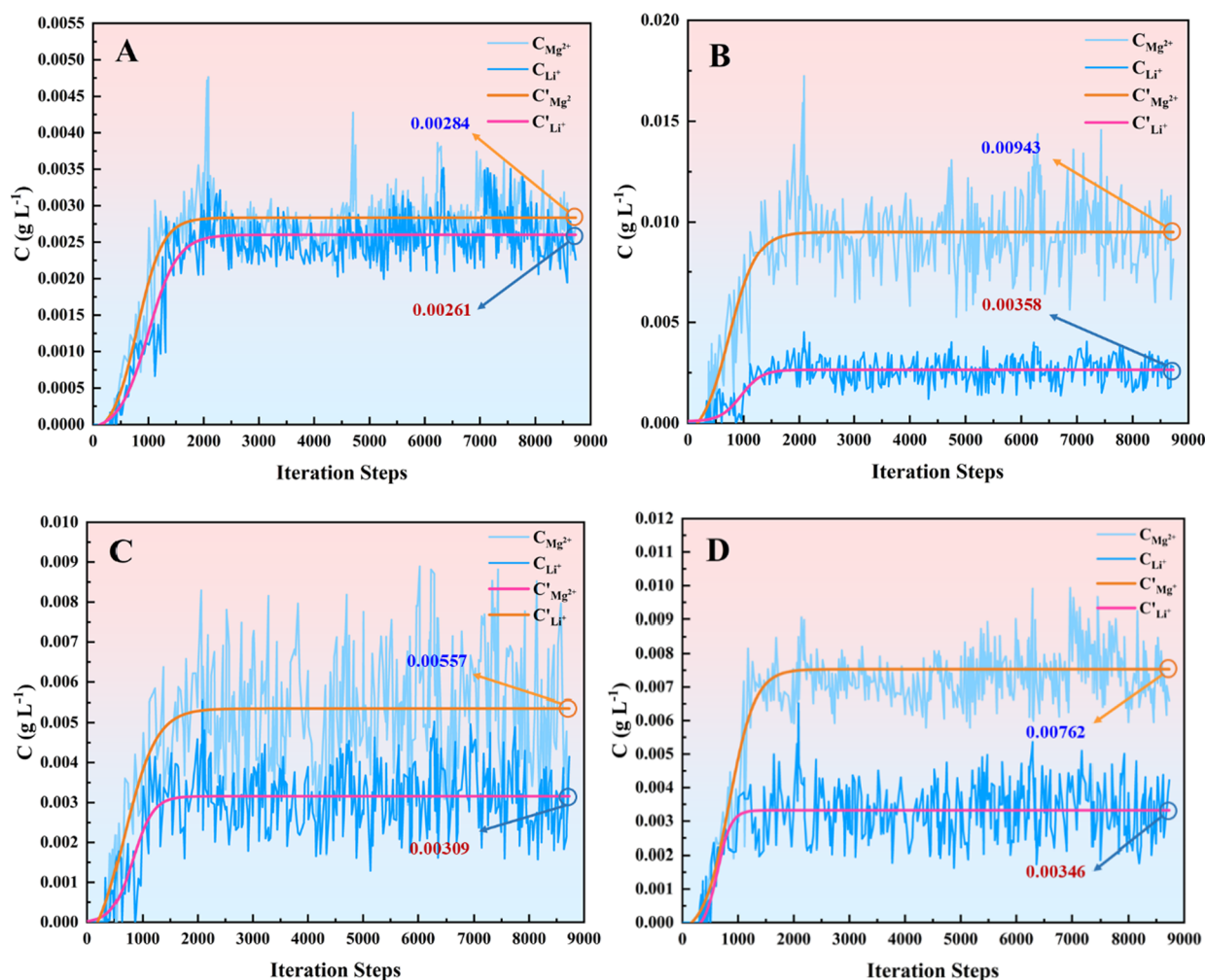


Figure 8. Concentration curve of magnesium–lithium ion in the NF process: (A) NF 90; (B) NF 270; (C) DK; (D) DL.

total number of grid divisions was 3,046,628, with a maximum grid quality of 0.98 and a minimum of 0.26. In the structural design of the membrane module, the effective area of the model was 24 cm² (6 cm in length, 4 cm in width), and the surface areas of the feed and concentrate outlets were 0.125 cm², while the permeate outlet surface area was 0.031 cm² (Figure 4). The heights of the upper and lower drainage chambers were set at 0.1 cm. Boundary conditions were defined as follows: the inlet was given a fixed velocity of 0.017 m/s and a solute concentration of 0.0336 kg/s. The outlet was considered as having fully developed flow, with zero derivatives of velocity components and solute concentration in all directions. The boundary conditions on the membrane surface were set as a no-slip wall, and an area with a refined grid was established near the membrane surface to facilitate source phase addition. The addition of the source phase was accomplished through the use of custom functions provided by Fluent software.

In the velocity field distribution map and turbulence kinetic energy map (Figure 5), the variation trends of the solution velocity field and ion concentration field in the free space above the membrane contribute to the optimization design of the subsequent NF process. The phenomenon indicates that when the solution enters the narrow space at the inlet and outlet, the kinetic energy of the solution molecules is relatively high. As the solution molecules collide with the NF membrane

in the confined space, their direction changes, resulting in a turbulent state of the fluid. Under the influence of shear flow, the closer to the stationary surface of the membrane, the slower the solution flow velocity.

In concentration-driven NF, solutes are transported from regions of high concentration to low concentration, achieving separation through the driving force of concentration gradients. Figures 6 and 7 illustrate the concentration field distribution maps of magnesium and lithium ions in the $x/X = 0$ cross-section. It is observed that magnesium ions accumulate more significantly on the concentrated side, while their concentration remains relatively low on the permeate side, indicating substantial retention of magnesium ions. In contrast, lithium ions exhibit a more uniform distribution overall, with noticeable variations primarily on the permeate side, highlighting the effective separation of magnesium and lithium ions.

Figure 8 depicts the concentration curves of magnesium and lithium ions during the NF process. The results indicate that, after reaching a stable state in the mass transfer process, the concentrations of magnesium and lithium ions on the permeate side fluctuate within a certain range. The simulated concentration values obtained by fitting the concentration curves are consistently lower than the experimental values, with a relative error (δ) within 5.5%. Despite this small deviation, it demonstrates that the DSPM-DE mathematical model can

effectively describe the mass transfer process. The simulation results closely resemble the experimental data, validating the accuracy of the simulation. The reason for these simulated results lies in the fact that the radius of lithium ions (0.238 nm) is smaller than that of magnesium ions (0.347 nm). Consequently, during membrane passage, lithium ions preferentially pass through and exhibit lower retention during the separation process, resulting in a smaller concentration difference on both sides of the membrane. The accumulation of magnesium ions on the concentrated solution side is driven by the pressure difference across the membrane, and due to differences in self-diffusion ability and activation energy, the concentration difference on both sides of the membrane is higher for magnesium ions.

4. CONCLUSIONS

This study employs an advanced mass transfer model to predict the flow and transport processes of magnesium and lithium ions in porous media within salt lakes, considering diffusion, electromigration, and convection of ions in membrane pores. Initially, membrane structural characteristics were understood during the characterization of four NF membranes to obtain fixed membrane parameters. Subsequently, a transport model equation was reasonably constructed through cross-flow retention experiments and numerical calculations. Finally, fluid dynamics calculations were performed using the finite element method based on model parameters, providing a detailed depiction of flow characteristics within the membrane assembly. This visualization effectively represents the transport process, confirming the consistency between the model and the actual transport phenomena. Additionally, the accuracy of the model was validated for magnesium–lithium separation predictions, with a deviation of less than 5.5%, through the simulation of velocity and concentration fields. The results demonstrate the precision of the established model in predicting outlet ion concentrations and retention rates in the cross-flow module, affirming the accuracy of the model in predicting these parameters.

AUTHOR INFORMATION

Corresponding Authors

Shaohua Yin – Faculty of Metallurgical and Energy Engineering, Kunming University of Science and Technology, Kunming, Yunnan 650093, China; orcid.org/0000-0003-2605-2442; Email: yinsh@kust.edu.cn

Shiwei Li – Faculty of Metallurgical and Energy Engineering, Kunming University of Science and Technology, Kunming, Yunnan 650093, China; Email: lswei11@163.com

Authors

Yueyu Liu – Faculty of Metallurgical and Energy Engineering, Kunming University of Science and Technology, Kunming, Yunnan 650093, China

Tingting Li – Faculty of Metallurgical and Energy Engineering, Kunming University of Science and Technology, Kunming, Yunnan 650093, China

Qing Guo – Faculty of Metallurgical and Energy Engineering, Kunming University of Science and Technology, Kunming, Yunnan 650093, China

Lili Gao – Faculty of Metallurgical and Energy Engineering, Kunming University of Science and Technology, Kunming, Yunnan 650093, China

Complete contact information is available at:

<https://pubs.acs.org/10.1021/acsomega.4c00246>

Notes

The authors declare no competing financial interest.

ACKNOWLEDGMENTS

Financial aid from the following programs is gratefully acknowledged: National Key Research and Development Program (grant number 2021YFC2901300).

NOMENCLATURE

$C_{i,f}$	feed concentration of ion i , g L ⁻¹
$C_{i,p}$	permeate concentration of ion i , g L ⁻¹
I	ionic strength, mol m ⁻³
F	Faraday constant, C mol ⁻¹
j_i	ionic flux of ion i , mol m ⁻² s ⁻¹
j_v	volumetric permeation flux, L m ⁻² h ⁻¹
K'_{2eff}	dimensionless coefficient
k_a	mass transfer coefficient, × 10 ⁻⁵ m s ⁻¹
$R_{i,int}$	intrinsic rejection of ion i dimensionless
$R_{i,obs}$	experimental rejection of ion i dimensionless
r_B	Bjerrum radius, m
r_i	Stokes radius, m
x	axial coordinate in the membrane, m
z_i	valence of ion
χ	membrane charge density, mol m ⁻³
δ	effective membrane thickness, accounting for tortuosity and porosity, m
$\Delta\Psi_D$	dimensionless Donnan potential
Ψ	electric potential, V
κ^{-1}	Debye length, m
ΔW	dimensionless excess solvation energy
0^-	feed/membrane interface, feed side
0^+	feed/membrane interface, membrane side
δ^-	membrane/permeate interface, membrane side
δ^+	membrane/permeate interface, permeate side

REFERENCES

- Zhang, Y.; Wang, L.; Sun, W.; Hu, Y.; Tang, H. Membrane technologies for Li⁺/Mg²⁺ separation from salt-lake brines and seawater: A comprehensive review. *J. Ind. Eng. Chem.* **2020**, *81*, 7–23.
- Barbosa, J. C.; Goncalves, R.; Costa, C. M.; Lanceros-Mendez, S. Toward Sustainable Solid Polymer Electrolytes for Lithium-Ion Batteries. *ACS Omega* **2022**, *7* (17), 14457–14464.
- Ashraf, M. A.; Usman, M.; Hussain, I.; Ahmad, F.; Guo, S.; Zhang, L. Lithium extraction from high magnesium salt lake brine with an integrated membrane technology. *Sep. Purif. Technol.* **2022**, *302*, No. 122163.
- Li, Y.; Wang, M.; Xiang, X.; Zhao, Y. J.; Peng, Z. J. Separation performance and fouling analyses of nanofiltration membrane for lithium extraction from salt lake brine. *J. Water Process* **2023**, *54*, No. 104009.
- Li, Y.; Zhao, Y.; Wang, H.; Wang, M. The application of nanofiltration membrane for recovering lithium from salt lake brine. *Desalination* **2019**, *468*, No. 114081.
- Divakar, S.; Padaki, M.; Balakrishna, R. G. Review on Liquid-Liquid Separation by Membrane Filtration. *ACS Omega* **2022**, *7* (49), 44495–44506.
- Soyekwo, F.; Wen, H.; Liao, D.; Liu, C. Fouling-resistant ionic graft-polyamide nanofiltration membrane with improved permeance for lithium separation from MgCl₂/LiCl mixtures. *J. Membr. Sci.* **2022**, *659*, No. 120773.
- Kumar, M.; Khan, M. A.; Arafat, H. A. Recent Developments in the Rational Fabrication of Thin Film Nanocomposite Membranes for

Water Purification and Desalination. *ACS Omega* **2020**, *5* (8), 3792–3800.

(9) Yang, Z.; Fang, W.; Wang, Z.; Zhang, R.; Zhu, Y.; Jin, J. Dual-skin layer nanofiltration membranes for highly selective $\text{Li}^+/\text{Mg}^{2+}$ separation. *J. Membr. Sci.* **2021**, *620*, No. 118862.

(10) Peng, H.; Zhao, Q. A Nano-Heterogeneous Membrane for Efficient Separation of Lithium from High Magnesium/Lithium Ratio Brine. *Adv. Funct. Mater.* **2021**, *31* (14), No. 2009430.

(11) Ni, H.; Wang, N.; Yang, Y.; Shen, M.; An, Q.-F. Positively-charged nanofiltration membrane constructed by polyethyleneimine/layered double hydroxide for $\text{Mg}^{2+}/\text{Li}^+$ separation. *Desalination* **2023**, *548*, No. 116256.

(12) Bowen, W. R.; Mukhtar, H. Characterisation and prediction of separation performance of nanofiltration membranes. *J. Membr. Sci.* **1996**, *112*, 263.

(13) Lavania, J.; Rastogi, N. K.; Balaraman, M.; Rangaswamy, S. Nonlinear Flux-Pressure Behavior of Solvent Permeation through a Hydrophobic Nanofiltration Membrane. *ACS Omega* **2021**, *6* (41), 27052–27061.

(14) Schaep, J.; Vandecasteele, C.; Mohammad, A. W.; Bowen, W. R. Analysis of the salt retention of nanofiltration membranes using the Donnan-steric partitioning pore model. *Sep. Sci. Technol.* **1999**, *34* (15), 3009–3030.

(15) Schaep, J.; Vandecasteele, C.; Mohammad, A. W.; Bowen, W. R. Modelling the retention of ionic components for different nanofiltration membranes. *Sep. Purif. Technol.* **2001**, *22–3* (1–3), 169–179.

(16) Yaroshchuk, A. E. Dielectric exclusion of ions from membranes. *Adv. Colloid Interface Sci.* **2000**, *85* (2–3), 193–230.

(17) Bandini, S.; Vezzani, D. Nanofiltration modeling: the role of dielectric exclusion in membrane characterization. *Chem. Eng. Sci.* **2003**, *58* (15), 3303–3326.

(18) Liu, Y.; Sipe, J. M.; Xu, W.; Zhu, X.; Bai, L.; Xu, D.; Li, G.; Liang, H.; Wiesner, M. R. Study on the mechanisms for the influence of nanomaterials on the separation performance of nanocomposite membrane from a modeling perspective. *Desalination* **2022**, *532*, No. 115740, DOI: 10.1016/j.desal.2022.115740.

(19) Li, Y. H.; Gregory, S. Diffusion of ions in sea water and in deep-sea sediments. *Geochim* **1974**, *38* (5), 703–714.

(20) Van der Bruggen, B.; Vandecasteele, C. Modelling of the retention of uncharged molecules with nanofiltration. *Water Res.* **2002**, *36* (5), 1360–1368.

(21) Ryzhkov, I. I.; Minakov, A. V. Theoretical study of electrolyte transport in nanofiltration membranes with constant surface potential/charge density. *J. Membr. Sci.* **2016**, *520*, 515–528.

(22) Vezzani, D.; Bandini, S. Donnan equilibrium and dielectric exclusion for characterization of nanofiltration membranes. *Desalination* **2002**, *149* (1–3), 477–483.

(23) Fadaei, F.; Hoshyargar, V.; Shirazian, S.; Ashrafizadeh, S. N. Mass transfer simulation of ion separation by nanofiltration considering electrical and dielectrical effects. *Desalination* **2012**, *284*, 316–323.